Investigating the Effect of Metal Nuclearity on Activity for Ethylene Hydrogenation by Metal-Organic-Framework-Supported oxy-Ni(II) Catalysts

Qining Wang [a], Zihan Pengmei [c], Riddhish Pandharkar [c], Laura Gagliardi [d], Joseph T. Hupp [a,*], Justin M. Notestein [b,*]

[a] Department of Chemistry, Northwestern University, 2145 Sheridan Rd., Evanston, IL 60208, United States

[b] Department of Chemical and Biological Engineering, Northwestern University, 2145 Sheridan Road, Evanston, IL 60208, United States

[c] Department of Chemistry, University of Chicago, 5735 S Ellis Ave, Chicago, IL 60637, United States

[d] Department of Chemistry, Pritzker School of Molecular Engineering, James Franck Institute, Chicago Center for Theoretical Chemistry, University of Chicago, 5735 S Ellis Ave, Chicago, IL 60637, United States; Argonne National Laboratory, Lemont, IL 60439, United States

[*] Email: j-hupp@northwestern.edu, j-notestein@northwestern.edu

Abstract

Metal-organic frameworks (MOFs), thanks to their well-defined coordination sites, are promising for studying catalytically active structures. To understand the effect of metal nuclearity in MOF-supported catalysts, we adjusted the nuclearity of oxy-Ni(II) supported on the zirconia-like nodes of MOF NU-1000 by modulating the Ni loading, where the organic linkers served to prevent node-to-node migration of grafted nickel ions. At the single-node level, we grafted auxiliary structural linkers, naphthalene dicarboxylate, to reduce the number of binding/grafting sites. We found higher catalytic rates at higher Ni loading for ethylene hydrogenation on a per-nickel-ion basis, despite the similar chemical environment of Ni(II) at different loadings; catalysts consisting mainly of pairs of nickel ions were more reactive than those of single nickel ions. These observations illustrate the need for at least two proximal nickel ions for effective catalysis – presumably one for hydrogen binding and heterolytic splitting and one for ethylene binding and activation.

Highlights

- A metal-organic framework (MOF) was used to systematically modulate the nuclearity of oxo-Ni(II) catalysts
- Multinuclear Ni species exhibited higher rates for ethylene hydrogenation than single-Ni species
- Ni species of higher nuclearity accelerated reactions by providing additional coordination sites for reaction intermediates

Graphical Abstract

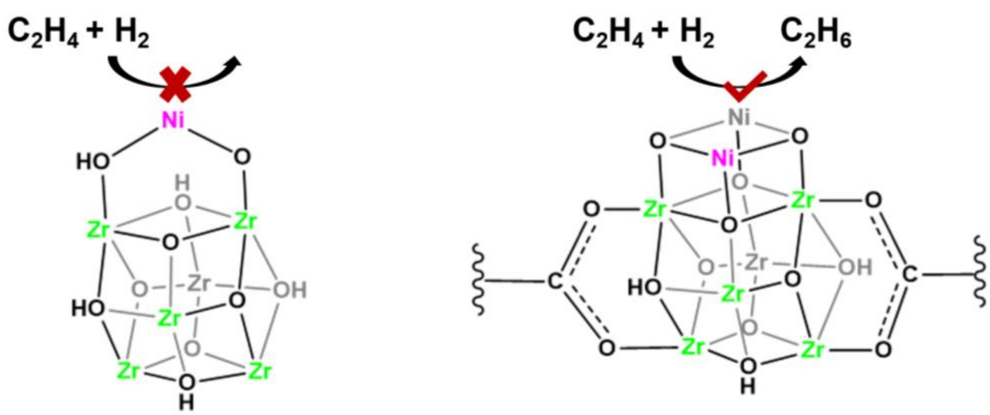

Keywords: metal-organic frameworks, MOFs, nickel catalysts, ethylene hydrogenation, catalyst nuclearity, active sites

1. Introduction

A widely implemented strategy to synthesize solid-state catalysts is to disperse catalytic species onto a solid support. Downsizing the particles of the catalytic species is generally desirable, as smaller particles and clusters present more defect sites that can increase catalytic activities.[1] Single-atom catalysts (SACs), the smallest achievable catalytic species, are thus of significant interest in realizing high catalytic activities. However, several underlying trade-offs can hinder SACs from achieving good catalytic performance. The high surface energies endow the SACs with high tendencies to aggregation and deactivation.[2] In addition, SACs may be mechanistically prevented from certain types of catalysis. As a prominent example, single-atom Pt supported on α-MoC exhibits lower water-gas-shift activity than catalysts where sub-nanometer Pt clusters are present. It was found that the crowding of surface Pt species can more promptly remove surface oxygen species, preventing the support from deep oxidation and deactivation.[2, 3] Those precedents illustrate the importance of understanding the interplay between the nuclearity of catalysts and catalytic activity, as it will provide crucial insights into optimizing catalytic systems.

Metal-organic frameworks (MOFs) have been used as solid catalyst supports for dispersing catalytic species down to single ions. Constructed from metal ions or clusters (nodes) connected by polytopic organic moieties (linkers), MOFs typically possess high internal surface areas and porosities. Those features facilitate the uptake of reactants, diffusive transport of catalytic species, and the effective release of products. Moreover, thanks to the high tunability of MOFs, additional functionalities can be realized during synthesis or post-synthetically.[4] For instance, metal ions can be grafted to nodes via reactions with terminal nonstructural aqua and hydroxo ligands or triply-bridging hydroxo ligands (μ_3-OH), concomitant with the release of a fraction of the organic ligands from the metal precursor molecule.[5] Thus, for node-grafted metal ions to be rendered capable of binding and activating candidate reactants, it is typically necessary to follow grafting with a step that releases/replaces unreacted ligand(s) from the precursor molecule. For remnant precursor alkyl or amidinate ligands, repetitive steam-dosing is a common removal/replacement strategy.[6]

Alternatively, metal ions can be attached to MOF linkers via coordinate-covalent (typically chelating) metal-linker bond formation.[7, 8] Also known are variants where: a) catalytic metal ions are grafted via insertion between linker-node bonds, combined with recruitment of a nonstructural node ligand as a bridge between the added metal ion and the node (rarely encountered), [9, 10] or b) intact catalytic complexes are node-tethered in fully molecular forms via reactive substituents at the periphery of the complex (often encountered).[11, 12] Regardless of the catalyst immobilization scheme, the resistance of metal ions to transport across organic linkers, even at temperatures approaching MOF decomposition temperatures (*ca.* 350 to 450 ℃ for typical Zr-MOFs) [13, 14] serves to prevent node-to-node metal ion migration and catalyst sintering. Thus, the initially synthetically defined metal-ion nuclearity tends to be preserved throughout catalyst operation.[15, 16]

NU-1000 ($[Zr_6(\mu_3\text{-}O)_4(\mu_3\text{-}OH)_4(OH)_4(H_2O)_4(TBAPy)_2]_\infty$ (TBAPy = 1,3,6,8-(*p*-benzoate)pyrene)) is a mesoporous MOF constructed from Zr_6 nodes and tetra-anionic TBAPy linkers. It has been used to support metal-oxy and metal-sulfur species to catalyze a wide range of reactions, including olefin hydrogenation, [15, 17] alkene epoxidation, [18] oxidative propane dehydrogenation, [19] singlet-oxygen mediated dialkyl-sulfide oxygenation, [20, 21] olefin dimerization, [17, 22, 23] oligomerization, [24-26] or polymerization, [27, 28] CO oxidation, [6, 29] xylene isomerization, [30, 31] and electrochemically or photochemically driven water oxidation, [32-34] water reduction, [35-37] or aqueous nitrate reduction. [38, 39] Each Zr_6 node connects to 8 linkers and presents four additional pairs of -OH/-H_2O ligands, suitable for grafting metal ions or carboxylate-terminated auxiliary ligands. Also present, regardless of node connectivity, are four Brønsted-acidic μ_3-hydroxo ligands that can react with alcohols[40] or ammonia, [41] or that can participate independently, or in cooperation with terminal node-aqua and/or -hydroxo ligands, in metal-ion grafting. [6, 42] NU-1000 possesses 3 nm diameter hexagonal channels and 1 nm diameter triangular channels down the *c*-axis of the particle, as well as small (~0.8 nm) openings, *c*-pores, and c_1-pores, that lie in the *ab*-plane and laterally interconnect the aforementioned channels (Figure 1).

While many MOF-node-supported metal ions are proficient catalysts for various gas-phase reactions, the interplay between the metal nuclearity and reactivity is largely unexplored. On conventional metal oxide supports, SACs can be achieved at extremely low loading, [43] and the effect of catalyst coverage can be studied by gradually increasing the metal loading. [44] However, studying the progression of metal nuclearity from monomer to dimer and above is challenging on metal oxide supports due to polydispersed metal binding sites. In some metal-oxide-supported catalysts such as vanadium on zirconia, the target nuclearity is difficult to maintain due to the weak metal-support interactions. Vanadium species tend to migrate and form clusters of higher nuclearity. [45] In the meantime, the uniform metal nodes in MOF provide monodispersed binding sites to realize the progression of increasing nuclearity, while the spatial isolation created by the linkers effectively prevent sintering.

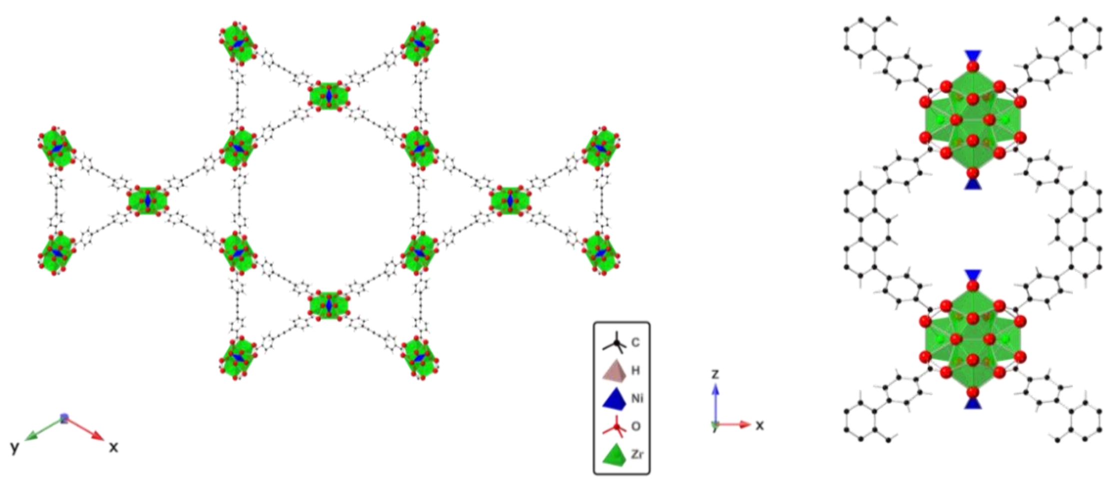

Figure 1. Single crystal structure of Ni supported on NU-1000. Blue pyramids show Ni residing in the c-pore.

In this work, Ni ions were deposited onto the Zr_6 nodes of formate-free NU-1000, and the effects of Ni nuclearity and siting were studied. According to the previously published single-crystal structure of Ni on NU-1000[46] (Figure 1), Ni ions preferentially reside in the c-pores of formate-containing NU-1000 single crystals. The effect of Ni residing in different locations in NU-1000 was therefore investigated by blocking the c-pores with naphthalenedicarboxylic acid (NDC), a ligand with similar aspect ratios as the c-pores. Using ethylene hydrogenation as the probe reaction, differences in reactivity arising from varied catalyst loadings and sitings were observed. The nature of the catalyst species was also studied with various spectroscopic techniques, where the presence of Ni-O-Ni sites was identified as crucial to the improved reactivity at high catalyst loadings.

2. Materials and Methods

2.1 Materials

All chemicals for the NU-1000 synthesis, namely 1,3,6,8-tetrabromopyrene, (4-(methoxycarbonyl)phenyl)boronic acid, tripotassium phosphate, tetrakis(triphenylphosphine) palladium(0), zirconyl chloride octahydrate, benzoic acid, hydrochloric acid, 1,4-dioxane, acetone, N,N-dimethylformamide, were purchased from Sigma Aldrich Chemicals Company, Inc. (Milwaukee, WI) and were used as received. The linker, 1,3,6,8-(p-benzoate)pyrene, was synthesized according to a reported procedure and its purity was confirmed via its ^1H NMR spectrum. For chemicals used in the deposition of Ni, bis(N,N''-di-t-butylacetamidinato)nickel(II) [$Ni(amd)_2$] was purchased from Strem Chemicals (Newbury Port, MA), and the anhydrous heptane was purified from HPLC grade heptane from Sigma Aldrich in a solvent purification system. Nitric acid, Ni and Zr ICP standards were purchased from Sigma Aldrich. Ultrapure deionized water (18.2 MB•cm resistivity) was obtained from a Millipore Milli-Q-Biocel A10 instrument (Millipore Inc., Billerica, MA). Deuterium oxide, deuterated sulfuric acid, and deuterated dimethyl sulfoxide used for ^1H NMR characterization were purchased from Sigma Aldrich and used as received. Deuterated sodium hydroxide was purchased from Sigma Aldrich and diluted with deuterium oxide to 0.1 M for NMR sample digestion.

2.2 Catalyst Synthesis

NU-1000, formate-free NU-1000 (NU-1000-FF). NU-1000 and NU-1000-FF were synthesized according to the published procedures.[47, 48] Upon thermal activation, the crystallinity of the obtained materials was confirmed by N_2 isotherm measurements at 77 K and PXRD. NU-1000-NDC was synthesized according to Peters et al.[49] with minor modification. The mixture of NU-1000 and NDC in DMF was held at 65°C for 12 hours. In addition, the HCl wash at 90°C was replaced by repeated DMF wash at 65°C every 30 min until all excess NDC ligands were removed. The amount of formate and NDC ligands were monitored by integrating the corresponding peaks in the ^1H NMR spectra (Figure S1-S3).

xNi (x= 0.044, 0.68, 0.86, 2.1, 3.6, 3.8) and 4.9Ni-NDC. Ni deposition was performed by adding NU-1000-FF to a heptane solution of $Ni(amd)_2$. An overall synthesis scheme is displayed in Figure 2. The preparation of precursor solutions and the addition of NU-1000-FF and NU-1000-NDC were performed in an Ar-filled glovebox. The amounts of $Ni(amd)_2$ added to 9.5 mL of heptane to achieve 0.5, 1, 2, 4, 6, 8 molar equivalence of 50 mg (0.021 mmol) FF-NU-1000 were 4.2 mg, 8.4 mg, 16.8 mg, 33.5 mg, 50.3 mg, and 67.2 mg, respectively. For 50 mg (0.021 mmol) NU-1000-NDC, 8 molar equivalence (67.2 mg) of $Ni(amd)_2$ was used. The reaction mixtures were subsequentially removed from the glovebox and transferred to a 70°C oven. After 16 hours, the reaction mixtures were removed from the oven and allowed to cool to room temperature. The samples were then solvent exchanged with heptane five times over a span of 24 hours. The catalysts were then dried in a vacuum oven at 70°C for one hour.

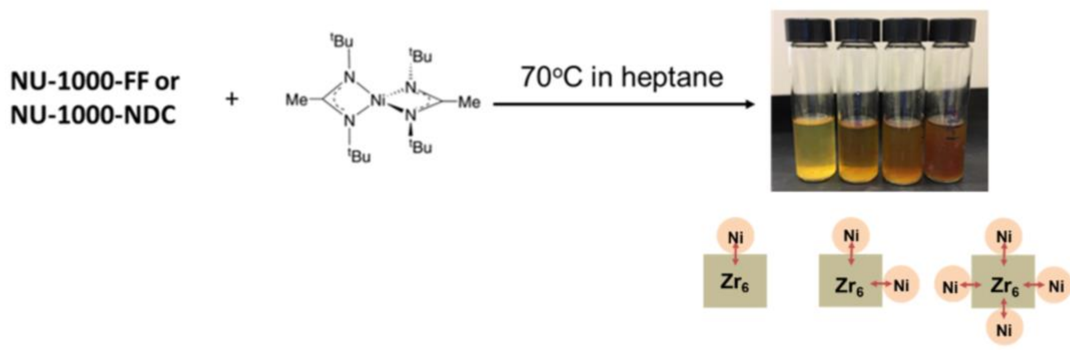

Figure 2. Synthesis of Ni supported on NU-1000-FF and NU-1000-NDC

2.3 Characterization

As-synthesized materials were first dried in a 70°C vacuum oven for one hour. The samples were then activated under high vacuum for 24 h using SmartVacPrep (Micromeritics, Norcross, GA) at 120 °C.

N_2 isotherms were measured afterwards using Micromeritics Tristar II 3020 at 77 K. Brunauer-Emmett-Teller (BET) surface area was determined at the range P/P0 = 0.005-0.1 and pore size distribution was calculated via density function theory (DFT) calculations using a carbon slit-pore model with a N2 kernel.

Inductively coupled plasma-optical emission spectroscopy (ICP-OES) was collected on Varian Vista-MDX model ICP-OES spectrometer (Varian, Walnut Creek, CA) with a CCD detector and Ar plasma that covers 175-785 nm range. MOF samples were prepared by dissolving 2-3 mg materials in 2 mL nitric acid in a 2-5 mL Biotage (Uppsala, Sweden) microwave vial. SPX microwave reactor (software version 2.3, build 6250) was used to heat the mixture at 150 °C for 15 min with stirring for complete digestion. 0.3 mL of the resulting mixtures were diluted to 10 mL with ultrapure deionized water and analyzed. For each sample, emissions at 231.604 and 221.647 nm for Ni, and 339.198, 343.823, and 327.305 nm for Zr, were compared to the standard solutions.

Powder X-ray diffraction (PXRD) patterns were recorded at room temperature on a STOESTADIMP powder diffractometer equipped with an asymmetric curved Germanium monochromator (Cu Kα1 radiation, λ = 1.54056 Å) and one-dimensional silicon strip detector (MYTHEN2 1K from DECTRIS). The generator was set to be 40 kV and 40 mA. The activated powder was measured in transmission geometry in a rotating holder with the intensity data from 1 to 20°. The scan step was set to be 2θ = 4°/min with 0.05° step width.

X-ray photoelectron spectra (XPS) were measured at Keck-II/NUANCE facility at Northwestern University using a Thermo Scientific ESCALAB 250 Xi (Al Kα radiation, 1486.6 eV). An equipped electron flood gun was utilized prior to any scans to minimize charging effect. Each spectrum was calibrated to C 1s peak at 284.8 eV.

X-ray absorption spectroscopy (XAS) measurements at the Ni K-edge (8777 eV) were performed on the insertion device beamline of DND-CAT (Sector 5-BMD), at the Advanced Photon Source (APS), Argonne National Laboratory. The beamline was detuned to 50% to minimize the presence of harmonics. Data were acquired in transmission in step-scan mode in about 15 min using ionization chambers optimized for the maximum current with linear response (~1010 photons detected/sec) with 10% absorption in the incident ion chamber and 70% absorption in the transmission X-ray detector. A Ni foil spectrum was acquired simultaneously with each sample measurement for energy calibration. Samples were pressed into aluminum plate holder with a thickness chosen to give an edge step of ~1.0.

^{1}H nuclear magnetic resonance (NMR) spectra were collected on a Bruker S4 Avance III 500 MHz system equipped with DCH CryoProbe and automated with a BACS-60 autosampler. Chemical shifts for ^{1}H spectra were referenced using internal solvent resonances and reported relative to tetramethylsilane (TMS). For NDC quantification, ~2 mg of sample was digested in 5 drops of D_2SO_4 followed by dilution in 0.6 mL d_6-DMSO. The number of scans was set to 32. The peak at 8.53 ppm was integrated for NDC quantification. For formate quantification, 10 drops of 0.1 M

$NaOD/D_2O$ solution was added to ~2 mg of sample, and the mixture was sonicated for 20 minutes. The mixture was then centrifuged, and the supernatant was further diluted with 0.5 mL of D_2O. The number of scans was set to 64. The peak at 8.38 ppm was integrated for formate quantification.

In Situ Diffuse Reflectance IR Fourier Transform Spectroscopy (DRIFTS) was performed at the Reactor Engineering and Catalyst Testing (REACT) core facility at Northwestern University. Approximately 10 mg of catalyst was diluted and ground with 100 mg of spectroscopic-grade KBr. The mixture was sealed into the praying mantis cell of a Thermo-iS50 infrared spectrometer. The sample was pretreated under an argon flow (100 sccm) at 200°C. A background spectrum was collected at this condition after one hour. The mixture was then cooled down to 150, 100, and 50°C. Background spectra were collected at each temperature point after one hour of stabilization. At 50°C, the mixture was exposed to 100 sccm 10% H_2/N_2, and difference spectra were recorded until there was no noticeable change from spectrum to spectrum. Then, the temperature was increased to 100, 150, and 200°C. 10 min of Ar purge was performed after each temperature ramp. At each temperature point, difference spectra were recorded until there was no noticeable change observed.

Thermogravimetric Analysis (TGA) was performed on a TA Q500 TGA instrument in a flow of 90 sccm 4% H_2/N_2 in high-res mode. The temperature was ramped from room temperature to 600°C at a ramp rate of 10°C/min.

2.4 Reactivity Studies

All reactivity studies were carried out using a packed bed reactor in the REACT core facility at Northwestern University. In a typical reaction, ~20 mg of catalyst was diluted with 1 g of silicon carbide (trace-metal grade) and packed in a quartz tube. The height of the bed was approximately 0.8 cm. The reaction temperature was controlled with a K-type thermocouple at the top of the catalyst bed. Pretreatments with 10% H_2/N_2 were carried out at 200°C for 12 h with a flow rate of

50 sccm, with a ramp rate of 10°C/min. Pressure in the reactor was monitored to be ~10 psig using a back-pressure regulator directly downstream from the reactor. To minimize the effect of the physiosorbed water and residual amd ligands, all catalysts were pre-treated in 50 sccm of 10% H_2 in N_2 at 200°C for 12 hours on stream prior to the introduction of reactant gases. After pretreatment, the temperatures were reduced to 50°C, and the reactant gases were then flowed over the sample. Reactant gases were 10% H_2/N_2 and 4% ethylene/N_2, and ethylene:H_2 was kept at 1:1. Products were analyzed via gas chromatography-flame ionization detection (GC-FID), and the gas mixture downstream were separated using a GS-Gaspro column (Agilent, 30m length, 0.32 mm diameter). Reaction rate was calculated by multiplying the molar flow rate by the conversion under each reaction condition and then normalizing to the moles of Ni (mol ethane*mol^{-1} Ni).

2.5 Calculations

Intermediates in the proposed reaction pathway were geometrically optimized in the electronic ground state using density functional theory (DFT) employing the M06-L functional[50] with the Gaussian 16 software package. Geometries were optimized using the def2-TZVP basis set[51, 52] on the nickel and zirconium atoms while the SDD pseudopotential[53] was applied on the zirconium atoms only. The def2-SVP basis set was assigned to the remaining C, H and O atoms. Collectively, these basis sets are referred to as *bs1*.

With the same level of theory and basis set, the frequency analysis was performed. Since the quintet was assumed to be the ground state, open-shell DFT formalism was used. Harmonic vibrational frequencies were computed and confirmed to have no imaginary values. For low frequency vibration modes, Grimme's entropy interpolation correction[54] was applied with the zero-point energy frequency correction factor of 0.976[55] to achieve the correct molecular thermochemical parameters. Since electronic energy is sensitive to the basis set quality, def2-TZVPP basis sets were assigned on the nickel and zirconium atoms while the SDD pseudopotential was applied on the zirconium atoms. The def2-TZVP basis set was assigned to the remaining C, H and O atoms. Collectively, these basis sets are referred to as *bs2*. Final Gibbs free energy values of single species were obtained by adding electronic energies from the M06-L/bs2 single point calculations and the corrected free energy correction under 473.15 K and 1.68 atm from M06-L/bs1 frequency analyses. Reaction free energies were obtained from the difference of the summed free energies of the products and reactants. In searching and optimizing of the transition state structures, the default Berny algorithm was applied with M06-L/*bs1*. After the procedure, a single imaginary frequency along the expectation direction was confirmed. Once a transition state was located, a single-point calculation was performed with M06-L/*bs2*.

3. Results and Discussions

3.1 Catalyst Characterizations

3.1.1 Physical Properties

The retention of crystallinity and porosity of the MOF catalysts were confirmed by PXRD (Figure 3) and N_2 physisorption (Figure 4). Other properties, including the BET surface areas, Ni loading by weight and per Zr_6 node quantified by ICP-OES, are summarized in Table 1. In formate-free NU-1000, Ni loading increases with an increase amount of precursor in solution and reaches 3.8 Ni per node, close to the maximum number of single-site cation sites that a Zr_6 node can accommodate (4). A decrease in BET surface area is generally observed as Ni loading increases. 1.4Ni is found to have lower-than-expected surface area, which is likely due to batch-to-batch variation in surface areas of the formate-free NU-1000.

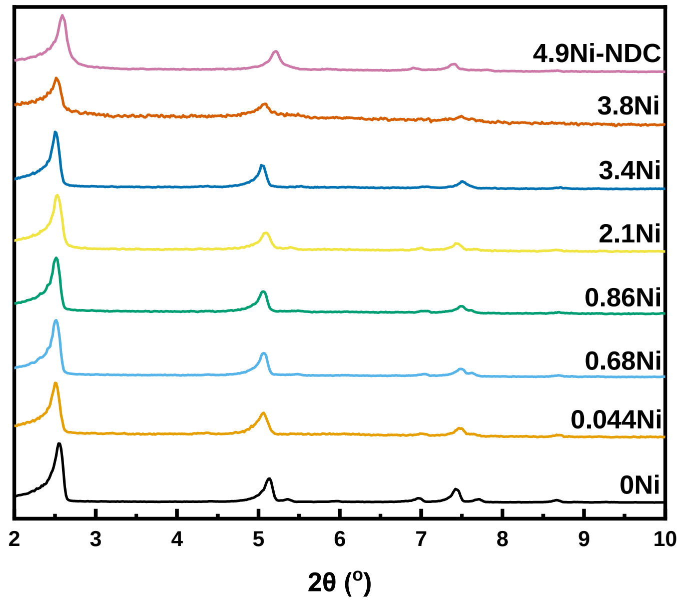

Figure 3. PXRD patterns of the as-made catalysts.

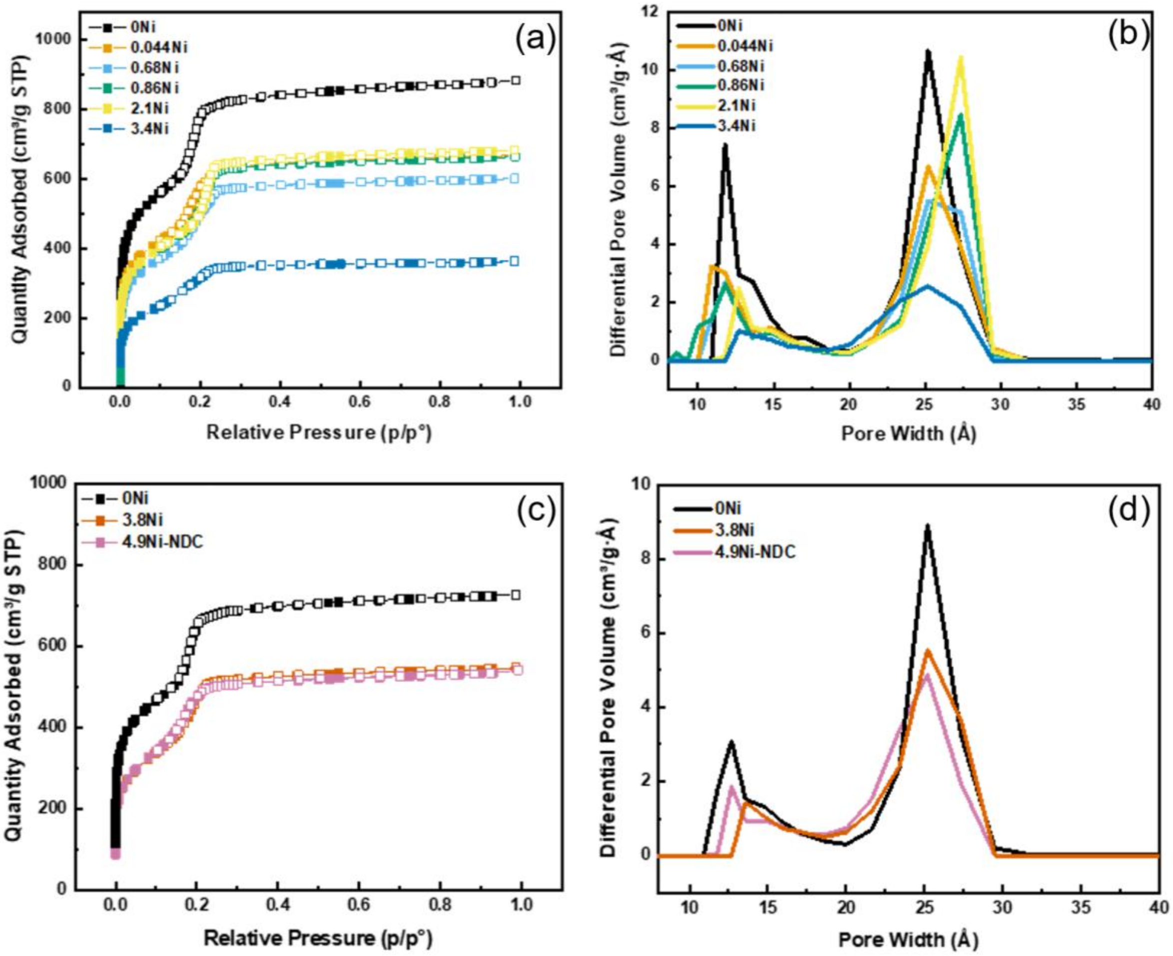

Figure 4. (a-b) N_2 isotherms and DFT differential pore size distributions of 0Ni~3.4Ni. (c-d) N_2 isotherms and DFT differential pore size distributions of 3.8Ni and 4.9Ni-NDC.

Table 1. Property table

Catalyst	**Ni(amd)$_2$ added**[a]	**Ni (wt%)**	**Ni/node**	**Ni/site**[b]	**Surface Area (m^2/g)**	**Pore Volumes (cm^3/g)**
0Ni	n/a	0	0	0	2166	7.2, 10.4
0.044Ni	0.5	0.067%	0.044	0.01	1632	3.3, 6.7
0.68Ni	1	1.3%	0.68	0.17	1425	2.7, 5.5
0.86Ni	2	1.7%	0.86	0.22	1536	2.6, 8.5
1.4Ni	2	2.8%	1.4	0.35	1281	2.6, 5.5
2.1Ni	4	2.5%	2.1	0.53	1539	2.5, 10.3
3.8Ni	8	5.4%	3.8	0.95	1262	1.4, 5.6
0Ni-NDC	n/a	0	0	0	1790	1.8, 8.8
4.9Ni-NDC	8	6.2%	4.9	2.5	1274	1.8, 4.9

[a] Molar equivalents Ni(amd)$_2$ per node added during synthesis

[b] Based on a theoretical 4 cation binding sites per node of NU-1000-FF and 2 cation binding sites per node of NU-1000-NDC.

3.1.2 Structural Investigations

In-situ DRIFTS confirmed the presence of amd ligands from the Ni precursor in the as-made catalysts (Figure 5). The spectra were collected at 200°C under 10% H_2, mimicking reaction conditions. While the introduction of H_2 did not perturb the spectra of 0Ni, various negative features emerged for the Ni catalysts. The sharp negative peak at 1630 cm^{-1} is present in all Ni-containing samples and is assigned to loss of the bending vibration of aqua groups. The negative feature at 3645 cm^{-1} in the spectra for 2.1Ni and 3.8Ni, and as a shoulder in 4.9Ni-NDC, is also attributed to the loss of aqua ligands. A negative feature centered at 3280 cm^{-1} is present in all Ni-containing samples; the peak is broadened and blue shifted for 4.9Ni-NDC. This feature arises from a combination of N-H from the amd ligands and O-H stretches on the nodes, both of which are perturbed by the H_2 treatment. The negative 2970 cm^{-1} peak is assigned to the C-H stretch of the t-butyl groups on the amd ligands. None of these features are present in the spectrum of 0Ni, showing that these aqua and hydroxyl groups affected by H_2 treatment at 200°C are associated with Ni atoms, as indicated in the structure shown in Figure 5. Overall, the DRITFS spectra confirmed the presence of amd ligands on Ni before catalysis, and that the amd ligands and aqua ligands on the nodes are perturbed thermally under reducing environment.

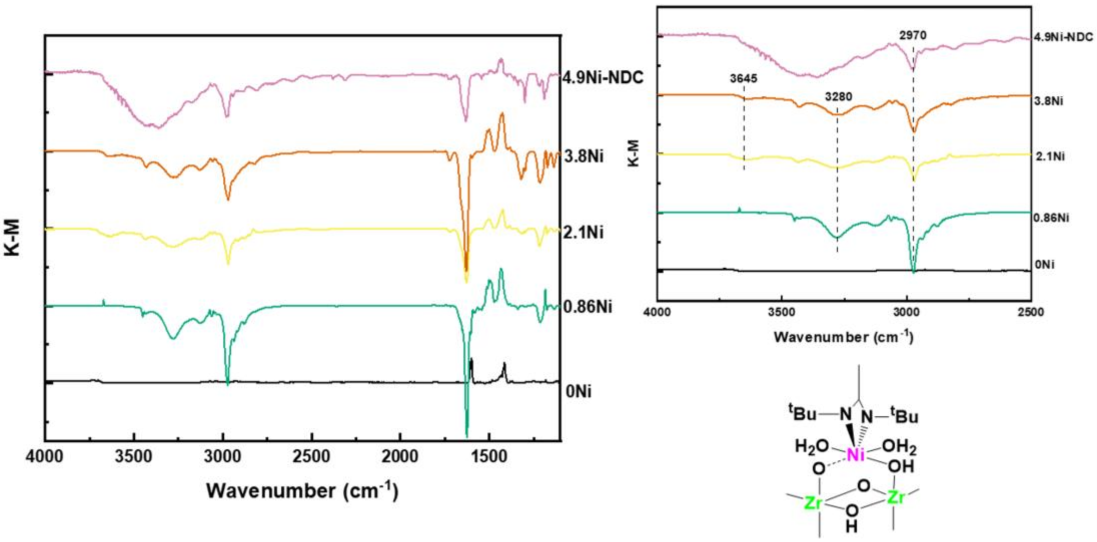

Figure 5. DRIFT spectra of 0Ni, 0.86Ni, 2.1Ni, 3.8Ni and 4.9Ni-NDC. Background spectra were collected following catalyst pretreatment in Ar at 200°C for 1 hour. The gas was then switched to 100 sccm 10% H_2/N_2 and difference spectra were collected until no further changes in spectra were observed.

The residual amd ligands and the degree of hydration of the catalysts were quantified with thermogravimetric analysis (TGA) in H_2 (Figure 6). Several stages of weight loss were observed in the TGA curves. Below 120°C, the weight losses originated from a combination of physisorbed water and the aqua ligands on the nodes, as suggested by the DRIFTS studies and TGA measurements on formate-free NU-1000. [48] 4.9Ni-NDC is significantly less hydrated than the rest of the samples (Table 2).

For the 0Ni sample, three distinct peaks at 50, 91, and 113°C were observed. The peaks for Ni-containing samples were less resolved, possibly because to the physisorbed water and the aqua ligands were removed rapidly and/or in a consecutive manner. In addition, the weight loss in the temperature range of 110~210°C only appeared in the Ni-containing samples and is assigned to the removal of the amd ligands, consistent with the amd ligand detachment temperature observed for $Ni(amd)_2$ deposited on SiO_2 films.[56] For Ni supported on NU-1000-FF, one amd remained per Ni (Table 2), consistent with attachment reaction such that one of the two amd ligands in the precursor was replaced by the hydroxyl and bridging oxygens on the Zr_6 nodes, leaving the second amd ligand behind. 4.9Ni-NDC contains significantly fewer remaining amd ligands per Ni and lower water content. We interpret this as arising from a different Ni nuclearity, as illustrated in the proposed catalyst structures in Figure 8. The lower hydricity in 4.9Ni-NDC could be the result of -OH/H_2O being consumed as amd ligands hydrolyze and detach from Ni.

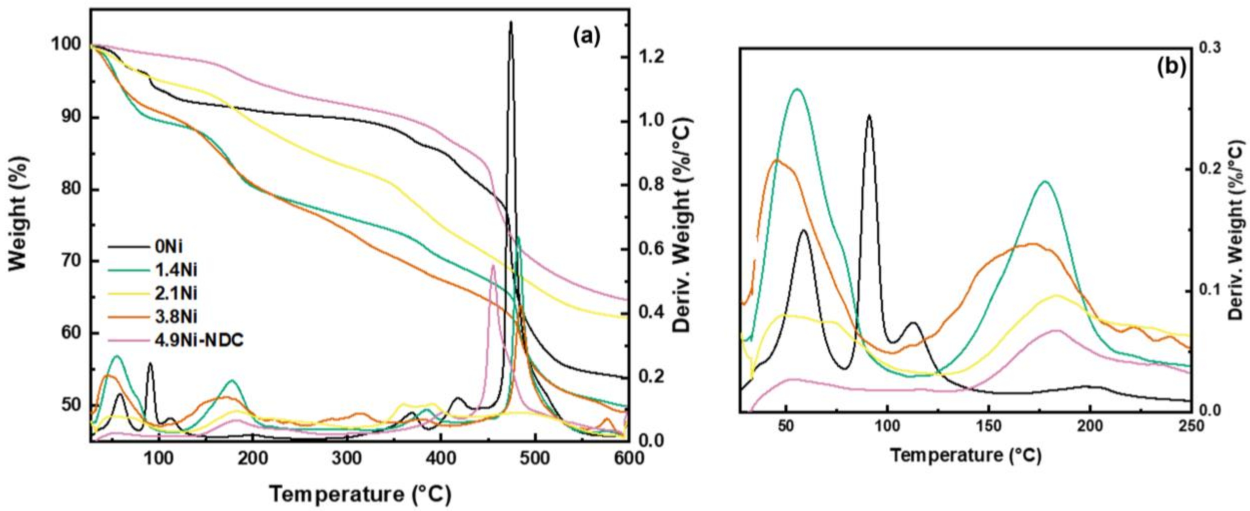

Figure 6. (a) Thermogravimetric analysis from 25-600°C. (b) Derivative weight curves from 24-250°C showing weight loss from physisorbed water and aqua ligands below ~125°C, and amd ligands at higher temperatures.

Table 2. Quantification of catalyst hydration and amd ligand remaining.

Sample	Water (wt.%)[a]	Ni (mmol/g)[b]	amd (mmol /g)[a]	amd:Ni
0Ni	7.70%	n/a	n/a	n/a
1.4Ni	10.2%	4.8	5.8	1.2
2.1Ni	5.35%	7.5	5.9	0.8
3.8Ni	9.70%	8.9	7.8	0.9
4.9Ni-NDC	1.29%	10.6	2.0	0.2

[a] from TGA
[b] from ICP-OES

The local coordination environments of Ni in 0.86Ni, 2.1Ni, 3.8Ni, and NDC-4.9Ni were studied with X-ray absorption (XAS). The Ni edge energies extracted from the X-ray absorption near edge structure (XANES) are centered at 8345.3 ± 0.1 eV for all samples (Table 3), shifted slightly from that of $Ni(OH)_2$ at 8346.9 eV. The pre-edge feature at 8333.5 eV is also present in all the spectra, which is assigned to the Ni 1s → 3d transition for octahedrally coordinated Ni^{2+}

species. The octahedral coordination of Ni^{2+} in all Ni-containing samples is confirmed by the first-shell EXAFS fittings, where the Ni-X (X = N or O) coordination numbers were extracted from fitting against the Ni-O scattering path of the $Ni(OH)_2$ standard (Table 3). Overall, Ni exhibits similar local chemical environment in all catalysts, consistent with the similar binding energies of Ni and Zr observed in XPS (Figure S4). However, the second-shell EXAFS fitting results reveal significant Ni-O-Ni contribution for 4.9Ni-NDC, where each Ni is bridged to approximately two other Ni by two oxygens, while Ni in the other catalysts remain isolated. Detailed fitting parameters can be found in Figure S6, S7, and Table S2. This is consistent with the overall stoichiometry reported in Table 1.

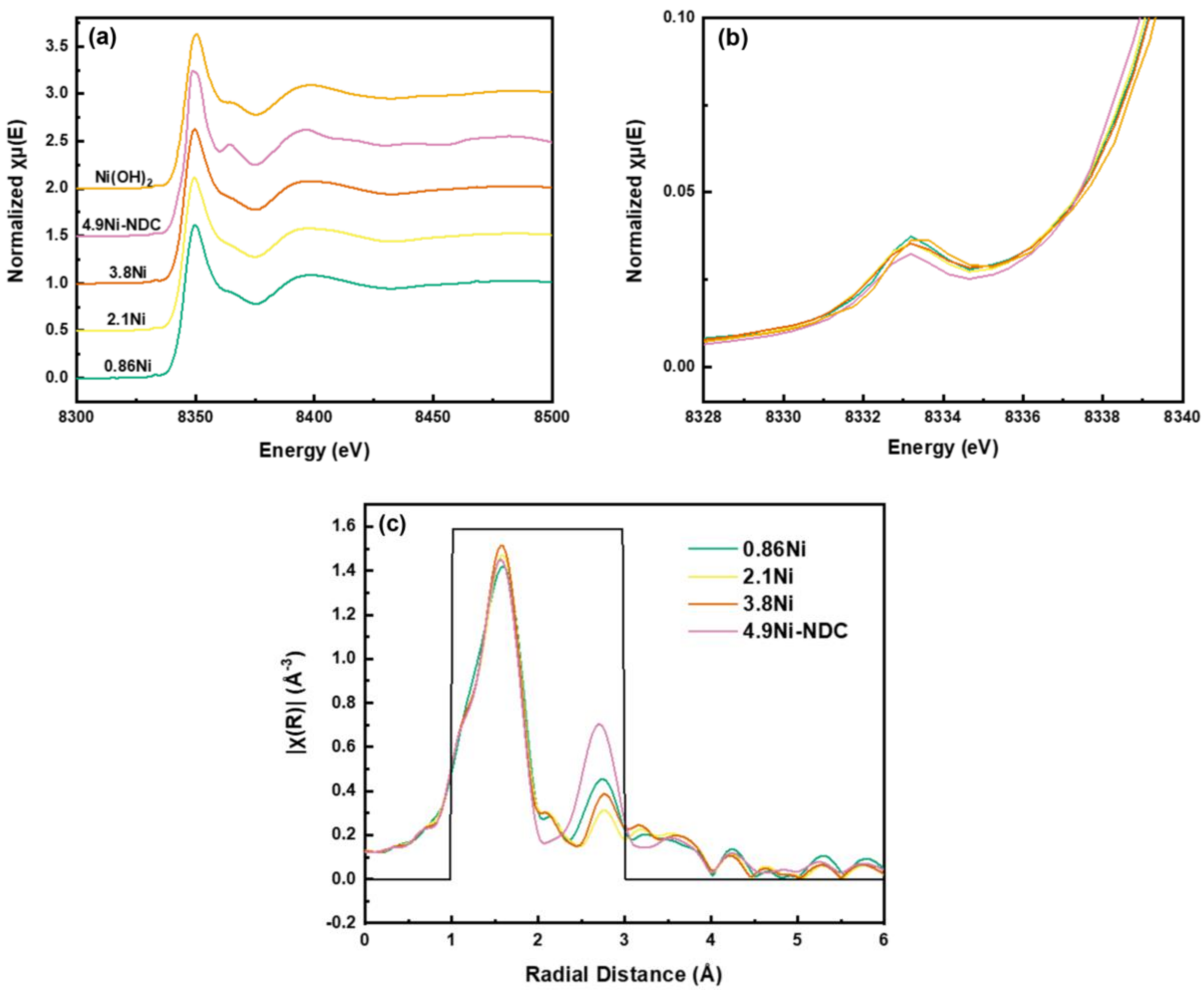

Figure 7. (a) XANES of 0.86Ni, 2.1Ni, 3.8Ni, 4.9Ni-NDC, and $Ni(OH)_2$ standard. (b) Pre-edge features at 8333.5 eV. (c) EXAFS in r-space with the fitting window shown in black.

Table 3. Ni K edge EXAFS fitting results.

Sample	Edge Energy	Ni-X R (Å)[a]	Ni-X N[a]	Ni-X σ^{2a}	Ni..Ni R (Å)[b]	Ni..Ni N[b,c]	Ni..Ni σ^{2b}
0.86Ni	8345.36	2.052 ± 0.002	6.4 ± 0.3	0.0085 ± 0.0004	3.067 ± 0.009	1.4 ± 0.7	0.0053 ± 0.0010
2.1Ni	8345.27	2.047 ± 0.003	6.5 ± 0.2	0.0077 ± 0.0005	3.101 ± 0.038	0.4 ± 0.2	0.0085 ± 0.0039
3.8Ni	8345.38	2.043 ± 0.003	6.5 ± 0.2	0.0072 ± 0.0005	3.040 ± 0.021	0.3 ± 0.1	0.0011 ± 0.0023
4.9Ni-NDC	8345.59	2.038 ± 0.002	6.7 ± 0.2	0.0077 ± 0.0004	3.033 ± 0.006	2.4 ± 0.2	0.0072 ± 0.0007

[a] Ni-X first shell bond distance (R), coordination number (N) and Debye-Waller factor
[b] Ni..Ni second-shell distance (R), number of scattering paths (N) and Debye-Waller factor
[c] possible contribution from Ni-O-Zr scattering in this low-loaded material

3.1.3 Proposed Active Site Structures

Based on the characterization discussed above, two catalyst structures are proposed in Figure 8. For Ni on formate-free NU-1000, octahedrally coordinated Ni ions reside on the -OH/H_2O ligand pairs of the Zr_6 nodes. In the case of Ni on NDC-NU-1000, Ni ions recruit the μ_3-O in addition to the -OH/H_2O ligands, resulting in the formation of Ni-O-Ni sites. Given a loading of 4.9 Ni per Zr_6 node on NDC-NU-1000, it is likely that there is also presence of Ni species of nuclearities higher than 2.

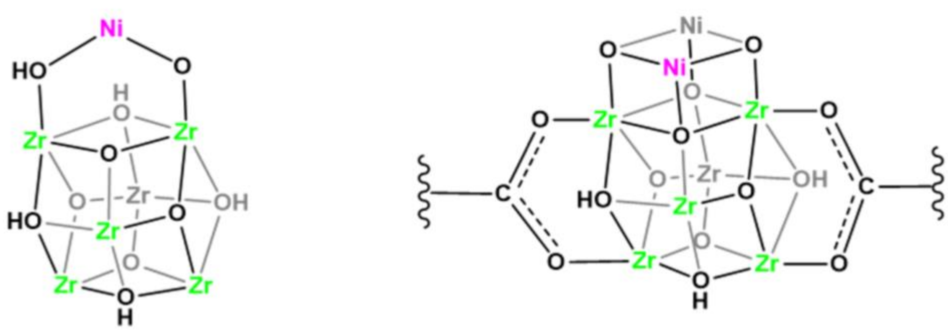

Figure 8. Representative, average, structures of Ni ions in formate-free NU-1000 (left) and in NDC-NU-1000 (right). Each node of NU-1000 contains up to three additional Ni atoms in similar coordination environments. The nodes of NDC-NU-1000 contain only one other binding site due to blocking by the NDC ligands. All Ni ions should be octahedrally coordinated; hydroxyl and/or precursor ligands on Ni ions are omitted for clarity.

3.2 Reactivity Studies

A representative conversion vs. time-on-stream plot is given for 3.8Ni in Figure 9(a), where conversion steadily increases over the temperature range of 55~95°C. The initially high reactivity at 55°C is due to Ni being saturated with hydride species after the H_2 pre-treatment. As this step is found to be the rate-determining step from the subsequent studies, a decrease in reactivity approaching steady state is expected. Figure 9(b) shows the rate at 150 °C for the studied catalysts. At loadings below 1 Ni per node, the rates are low and close to that of the bare NU-1000. Rates per Ni atom increase when the loading reaches 2.1 Ni per node and continue to increase for 3.4 Ni per node. The rates for 4.9Ni-NDC are close to ten-fold higher than that for 3.8Ni. However, further reactivity studies on 3.8Ni and 4.9Ni-NDC reveal reaction orders of 0.8 and ~0 for H_2 and ethylene, respectively (Figure 10), indicating that similar mechanisms operate on these two exemplar catalysts. Finally, the apparent activation energies extracted from the Arrhenius plots are 22 kcal/mol for 3.8Ni and 17 kcal/mol for 4.9Ni-NDC. We hypothesize that slightly higher activation energy observed for 3.8Ni could be the result of less Ni-O-Ni sites present at a lower Ni loading. The formation of new Ni-O-Ni sites from mobile Ni monomers with increasing temperatures in 3.8Ni could also be a potentially contributing factor.

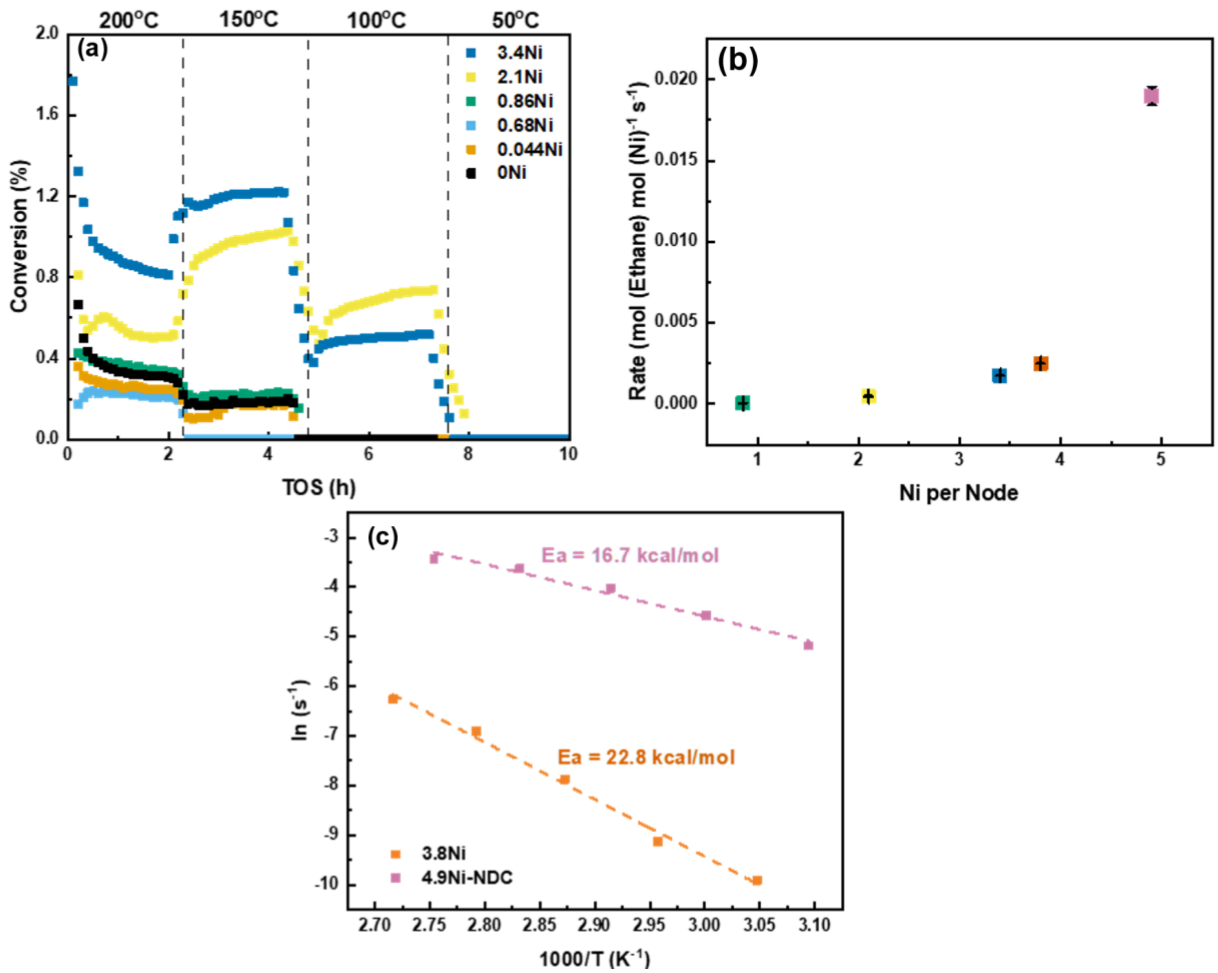

Figure 9. (a) Conversion vs. time on stream (TOS) for 3.8Ni at five temperatures. Conditions: ~20 mg catalyst diluted in 1 g of SiC, pre-treated in 50 sccm 10% H_2/N_2, 12 h at 200°C, followed by 1:1 H_2:C_2H_4 (10 sccm 10% H_2/N_2 and 25 sccm 4% ethylene/N_2). (b) Ni-normalized reaction rates at 150°C. (c) Arrhenius plots of 3.8Ni and 4.9Ni-NDC from 50-90°C.

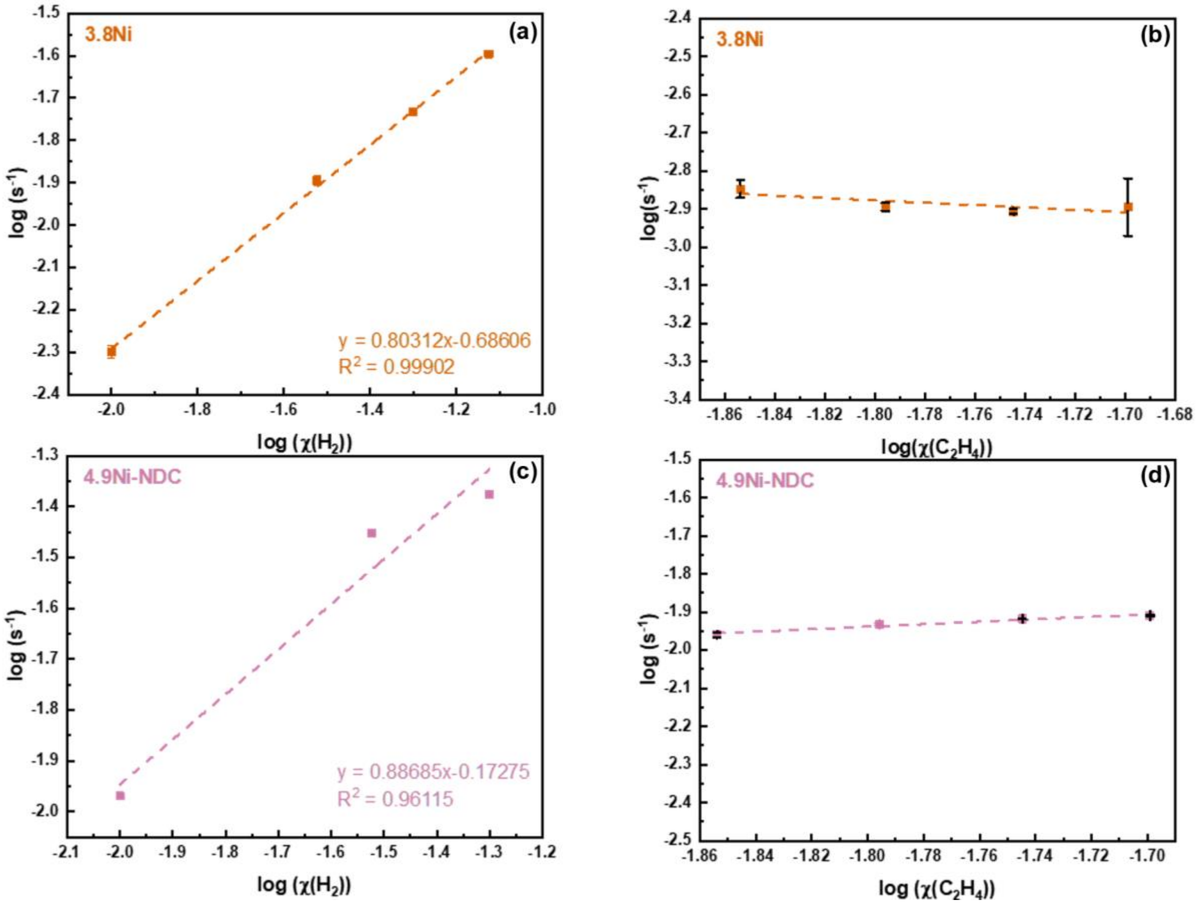

Figure 10. Reaction orders of H_2 and ethylene measured for (a)-(b) 3.8Ni, and (c)-(d) 4.9Ni-NDC at 100°C. H_2 reaction order measured at constant ethylene mole fraction of 0.01 and H_2 mole fraction varied from 0.01-0.075. Ethylene reaction order measured at constant H_2 mole fraction of 0.01 and ethylene mole fraction varied from 0.014-0.02.

3.3 Mechanistic Investigations via DFT

The mechanism for ethylene hydrogenation that has been studied with DFT for the mono-nickel case involves the heterolytic slitting of the H_2 followed by the formation of the nickel-hydride activated species. [15,46] We explore a similar mechanism for the dinickel case. We only study the catalytic cycle of the hydrogenation and the barriers involved in this reaction. The mechanisms for catalyst synthesis and catalyst activation are not studied. The relative free energies and enthalpies along the reaction are shown in Figure 11 and the absolute energies are reported in the SI.

Given the structure determined by EXAFS, we modeled an initial structure, such as might exist before the catalyst pretreatment, consisting of two Ni atoms linked by μ^3-O bridges with three aqua ligands surrounding each Ni atom. Three elementary steps were then studied (Figure 11 and Figure S11), namely the first C-H bond formation (step 1~2), and the second C-H bond formation (step 2~3) and catalyst regeneration/ H_2 splitting (step 5~6).

The Ni to the μ_3-O distances for the two Ni are 1.96 Å in the pristine di-Ni structure, where both Ni are fully coordinated with water ligands. Those distances are comparable to the 2.04 Å determined from the EXAFS fitting for 4.9Ni-NDC. Meanwhile, this distance was found to be 2.12 Å for the mono-Ni structure. Considering the distance between Ni and the O of the aqua ligands being 2.00 Å, the average Ni-O distance is also close to the 2.05 Å extracted from the EXAFS fitting for 0.86Ni.

In the previously proposed mechanism for the mono-nickel case, the heterolytic splitting of H_2 and the protonation of the ethyl group to make ethane needed to occur in one step because there is no other place for a proton to bond upon splitting. The presence of Ni_2-O_2 moiety in the di-nickel case, better accommodates this heterolytic splitting by forming a Ni-hydride and a hydroxy group. This is the active species of the catalyst. The reactant ethylene molecule adsorbs on the other Ni atom (that hasn't formed the hydride). Following the previous studies of the catalytic cycle,[46] this is used as the energy reference for the reported relative energies in Figure 11. The η^2-bound ethylene is only weakly activated at this stage with $d_{C\text{-}C}$ = 1.35 Å, as compared to 1.33 Å in free ethylene. This is followed by the migratory insertion of the hydride to form a nickel-ethyl species. This step has a free energy of activation of 12.7 kcal/mol. The subsequent attack of the adjacent proton to form the ethane has an activation free energy of 2.4 kcal/mol. The ethane is only weakly adsorbed on the Ni atom. The Ni-hydride starting species is regenerated when another H_2 molecule displaces the ethane and undergoes the subsequent heterolytic splitting of that has an apparent barrier – i.e. free energy of TS_{56} with respect to the bare structure (species 4) – of about 24 kcal/mol. This high apparent barrier (partly entropic as H_2 molecule is first adsorbed and partly enthalpic because the H_2 is split) might justify the experimental dependence of the rate on the H_2 activity. This, however, needs to be verified with further studies and kinetic modeling.

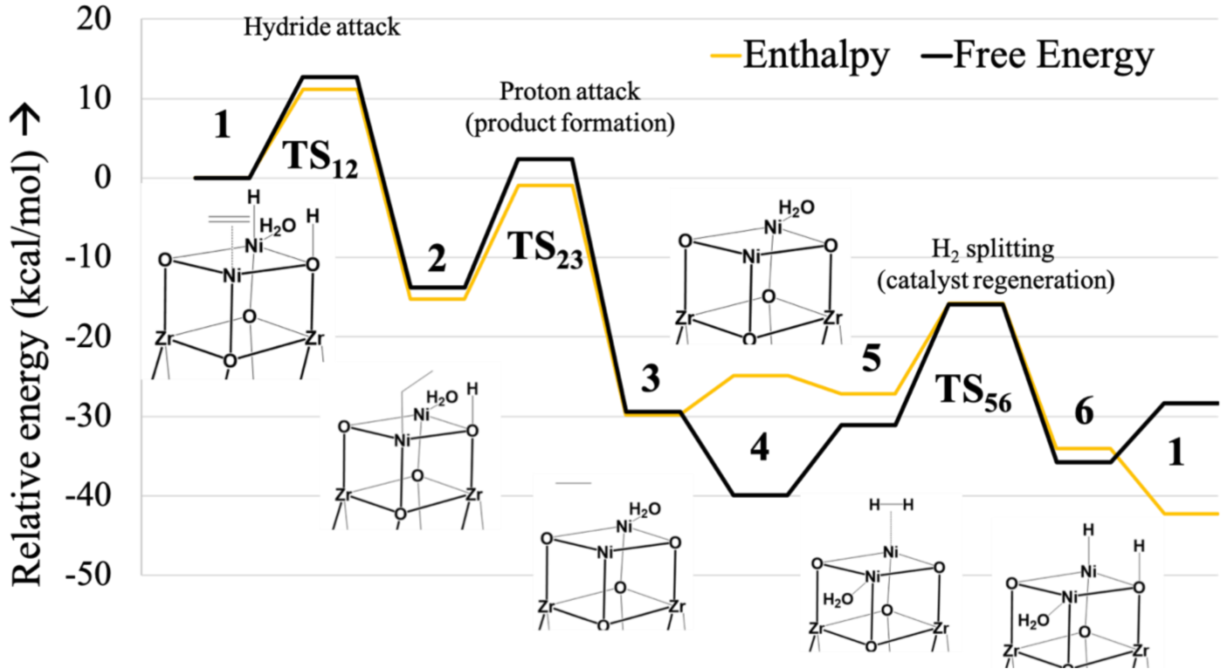

Figure 11. DFT-calculated enthalpies (yellow) and free energies (gray) for intermediates and transition state structures. Energies given in kcal/mol relative to species 1. The lower portion of the node and linkers bound to the Zr_6 nodes are omitted for clarity.

We also note that a mechanism exactly like the mono-nickel case was explored for the di-nickel catalyst – where one Ni is the active site, and the other Ni is a spectator. Intermediates for this mechanism were hard to obtain and would converge to one of the species reported mechanism. Another possibility of the H_2 splitting in a way to form Ni-hydride and protonating the the μ-O of the node (below the Ni) was also considered. This does not lead to product formation because the ethyl group (after the migratory insertion of the hydride) attaches to the other Ni and thus is too far from the proton for the reaction to complete. Both these mechanisms were thus discarded.

4. Conclusions

We found that the nuclearity of NiOx supported on MOF NU-1000 can be controlled by systematically adjusting the overall Ni loading. We are also able to increase NiOx nuclearity by introducing node-connecting auxiliary ligands (NDC anions) that change the Zr-MOF node from eight-connected to ten-connected and thus decrease the number of potential grafting sites presented by each node. The structural differences between mononuclear Ni cations and Ni-O-Ni sites are reflected in their different ethylene hydrogenation reactivities, where single-site Ni at loadings below 1 Ni per Zr_6 node is significantly less reactive. The most reactive catalyst is Ni supported on NDC-NU-1000, which is predominantly composed of Ni-O-Ni sites. Changing the catalyst loading and otherwise manipulating metal-ion nuclearity has a profound impact on the "per site" catalytic performance.

Acknowledgements

This work was supported as part of the Inorganometallic Catalyst Design Center, an EFRC funded by the U.S. Department of Energy (DOE), Office of Science, Office of Basic Energy Sciences (DE-SC0012702). This work made use of the J. B. Cohen X-ray Diffraction Facility supported by the MRSEC program of the National Science Foundation (DMR-1121262) at the Materials Research Center of Northwestern University. This work made use of the EPIC and Keck-II facilities of the NUANCE Center at Northwestern University, which has received support from the Soft and Hybrid Nanotechnology Experimental (SHyNE) Resource (NSF NNCI-1542205); the MRSEC program (NSF DMR-1121262) at the Materials Research Center; the International Institute for Nanotechnology (IIN); the Keck Foundation; and the State of Illinois, through the IIN. The REACT Core facility acknowledges funding from the U.S. Department of Energy, Office of Science, Office of Basic Energy Sciences, Catalysis Science program used for the purchase of the Nicolet 6700 FT-IR [DE-FG02-03ER15457] and BenchCAT reactor system [DE-SC0001329]. This work made use of the Advanced Photon Source of Argonne National Lab (ANL), at DND-CAT (Sector 5), which is supported by E.I. DuPont de Nemours & Co., Northwestern University, and The Dow Chemical Co.

Reference

1. Rong, H.; Ji, S.; Zhang, J.; Wang, D.; Li, Y., Synthetic strategies of supported atomic clusters for heterogeneous catalysis. *Nature Communications* **2020,** *11* (1), 5884.
2. Zhang, X.; Zhang, M.; Deng, Y.; Xu, M.; Artiglia, L.; Wen, W.; Gao, R.; Chen, B.; Yao, S.; Zhang, X.; Peng, M.; Yan, J.; Li, A.; Jiang, Z.; Gao, X.; Cao, S.; Yang, C.; Kropf, A. J.; Shi, J.; Xie, J.; Bi, M.; van Bokhoven, J. A.; Li, Y.-W.; Wen, X.; Flytzani-Stephanopoulos, M.; Shi, C.; Zhou, W.; Ma, D., A stable low-temperature H2-production catalyst by crowding Pt on α-MoC. *Nature* **2021,** *589* (7842), 396-401.
3. Ding, K.; Gulec, A.; Johnson, A. M.; Schweitzer, N. M.; Stucky, G. D.; Marks, L. D.; Stair, P. C., Identification of active sites in CO oxidation and water-gas shift over supported Pt catalysts. *Science* **2015,** *350* (6257), 189-192.
4. Yang, D.; Gates, B. C., Catalysis by Metal Organic Frameworks: Perspective and Suggestions for Future Research. *ACS Catalysis* **2019,** *9* (3), 1779-1798.
5. Otake, K.-i.; Ahn, S.; Knapp, J.; Hupp, J. T.; Notestein, J. M.; Farha, O. K., Vapor-Phase Cyclohexene Epoxidation by Single-Ion Fe(III) Sites in Metal–Organic Frameworks. *Inorganic Chemistry* **2021,** *60* (4), 2457-2463.
6. Yang, Y.; Zhang, X.; Kanchanakungwankul, S.; Lu, Z.; Noh, H.; Syed, Z. H.; Farha, O. K.; Truhlar, D. G.; Hupp, J. T., Unexpected "Spontaneous" Evolution of Catalytic, MOF-Supported Single Cu(II) Cations to Catalytic, MOF-Supported Cu(0) Nanoparticles. *Journal of the American Chemical Society* **2020,** *142* (50), 21169-21177.
7. Wang, C.; Xie, Z.; deKrafft, K. E.; Lin, W., Doping Metal–Organic Frameworks for Water Oxidation, Carbon Dioxide Reduction, and Organic Photocatalysis. *Journal of the American Chemical Society* **2011,** *133* (34), 13445-13454.
8. Manna, K.; Zhang, T.; Carboni, M.; Abney, C. W.; Lin, W., Salicylaldimine-Based Metal–Organic Framework Enabling Highly Active Olefin Hydrogenation with Iron and Cobalt Catalysts. *Journal of the American Chemical Society* **2014,** *136* (38), 13182-13185.
9. Liu, J.; Li, Z.; Zhang, X.; Otake, K.-i.; Zhang, L.; Peters, A. W.; Young, M. J.; Bedford, N. M.; Letourneau, S. P.; Mandia, D. J.; Elam, J. W.; Farha, O. K.; Hupp, J. T., Introducing Nonstructural Ligands to Zirconia-like Metal–Organic Framework Nodes To Tune the Activity of Node-Supported Nickel Catalysts for Ethylene Hydrogenation. *ACS Catalysis* **2019,** *9* (4), 3198-3207.
10. Yuan, S.; Chen, Y.-P.; Qin, J.; Lu, W.; Wang, X.; Zhang, Q.; Bosch, M.; Liu, T.-F.; Lian, X.; Zhou, H.-C., Cooperative Cluster Metalation and Ligand Migration in Zirconium Metal–Organic Frameworks. *Angewandte Chemie International Edition* **2015,** *54* (49), 14696-14700.
11. Peralta, R. A.; Huxley, M. T.; Evans, J. D.; Fallon, T.; Cao, H.; He, M.; Zhao, X. S.; Agnoli, S.; Sumby, C. J.; Doonan, C. J., Highly Active Gas Phase Organometallic Catalysis Supported Within Metal–Organic Framework Pores. *Journal of the American Chemical Society* **2020,** *142* (31), 13533-13543.
12. Momeni, M. R.; Pahls, D. R.; Yang, D.; Wang, T. C.; Farha, O. K.; Hupp, J. T.; Cramer, C. J.; Gagliardi, L.; Gates, B. C., Correction to "Metal–Organic Framework Nodes as Nearly Ideal Supports for Molecular Catalysts: NU-1000- and UiO-66-Supported Iridium Complexes". *Journal of the American Chemical Society* **2017,** *139* (50), 18406-18406.
13. Nguyen, L. H. T.; Nguyen, T. T. T.; Dang, Y. T.; Tran, P. H.; Le Hoang Doan, T., Microwave-Assisted Synthesis as an Efficient Method to Enhance the Catalytic Activity of Zr-Based Metal Organic

Framework UiO-66 in a Heterocyclization Reaction. *Asian Journal of Organic Chemistry* **2019,** *8* (12), 2276-2281.
14. Ramezanzadeh, M.; Tati, A.; Bahlakeh, G.; Ramezanzadeh, B., Construction of an epoxy composite coating with exceptional thermo-mechanical properties using Zr-based NH2-UiO-66 metal-organic framework (MOF): Experimental and DFT-D theoretical explorations. *Chemical Engineering Journal* **2021,** *408*, 127366.
15. Li, Z.; Schweitzer, N. M.; League, A. B.; Bernales, V.; Peters, A. W.; Getsoian, A. B.; Wang, T. C.; Miller, J. T.; Vjunov, A.; Fulton, J. L.; Lercher, J. A.; Cramer, C. J.; Gagliardi, L.; Hupp, J. T.; Farha, O. K., Sintering-Resistant Single-Site Nickel Catalyst Supported by Metal–Organic Framework. *Journal of the American Chemical Society* **2016,** *138* (6), 1977-1982.
16. Wu, X.; Zhang, H.; Zuo, S.; Dong, J.; Li, Y.; Zhang, J.; Han, Y., Engineering the Coordination Sphere of Isolated Active Sites to Explore the Intrinsic Activity in Single-Atom Catalysts. *Nano-Micro Letters* **2021,** *13* (1), 136.
17. Bernales, V.; Yang, D.; Yu, J.; Gümüşlü, G.; Cramer, C. J.; Gates, B. C.; Gagliardi, L., Molecular Rhodium Complexes Supported on the Metal-Oxide-Like Nodes of Metal Organic Frameworks and on Zeolite HY: Catalysts for Ethylene Hydrogenation and Dimerization. *ACS Applied Materials & Interfaces* **2017,** *9* (39), 33511-33520.
18. Ahn, S.; Thornburg, N. E.; Li, Z.; Wang, T. C.; Gallington, L. C.; Chapman, K. W.; Notestein, J. M.; Hupp, J. T.; Farha, O. K., Stable Metal–Organic Framework-Supported Niobium Catalysts. *Inorganic Chemistry* **2016,** *55* (22), 11954-11961.
19. Li, Z.; Peters, A. W.; Bernales, V.; Ortuño, M. A.; Schweitzer, N. M.; DeStefano, M. R.; Gallington, L. C.; Platero-Prats, A. E.; Chapman, K. W.; Cramer, C. J.; Gagliardi, L.; Hupp, J. T.; Farha, O. K., Metal–Organic Framework Supported Cobalt Catalysts for the Oxidative Dehydrogenation of Propane at Low Temperature. *ACS Central Science* **2017,** *3* (1), 31-38.
20. Hwang, Y. K.; Hong, D.-Y.; Chang, J.-S.; Seo, H.; Yoon, M.; Kim, J.; Jhung, S. H.; Serre, C.; Férey, G., Selective sulfoxidation of aryl sulfides by coordinatively unsaturated metal centers in chromium carboxylate MIL-101. *Applied Catalysis A: General* **2009,** *358* (2), 249-253.
21. Xie, M.-H.; Yang, X.-L.; Zou, C.; Wu, C.-D., A SnIV–Porphyrin-Based Metal–Organic Framework for the Selective Photo-Oxygenation of Phenol and Sulfides. *Inorganic Chemistry* **2011,** *50* (12), 5318-5320.
22. Redfern, L. R.; Lo, W.-S.; Dillingham, I. J.; Eatman, J. G.; Mian, M. R.; Tsung, C.-K.; Farha, O. K., Enhancing Four-Carbon Olefin Production from Acetylene over Copper Nanoparticles in Metal–Organic Frameworks. *ACS Applied Materials & Interfaces* **2020,** *12* (28), 31496-31502.
23. Chen, C.; Alalouni, M. R.; Dong, X.; Cao, Z.; Cheng, Q.; Zheng, L.; Meng, L.; Guan, C.; Liu, L.; Abou-Hamad, E.; Wang, J.; Shi, Z.; Huang, K.-W.; Cavallo, L.; Han, Y., Highly Active Heterogeneous Catalyst for Ethylene Dimerization Prepared by Selectively Doping Ni on the Surface of a Zeolitic Imidazolate Framework. *Journal of the American Chemical Society* **2021,** *143* (18), 7144-7153.
24. Joshi, R.; Saxena, A.; Gounder, R., Mechanistic insights into alkene chain growth reactions catalyzed by nickel active sites on ordered microporous and mesoporous supports. *Catalysis Science & Technology* **2020,** *10* (21), 7101-7123.
25. Liu, P.; Redekop, E.; Gao, X.; Liu, W.-C.; Olsbye, U.; Somorjai, G. A., Oligomerization of Light Olefins Catalyzed by Brønsted-Acidic Metal–Organic Framework-808. *Journal of the American Chemical Society* **2019,** *141* (29), 11557-11564.
26. Goetjen, T. A.; Zhang, X.; Liu, J.; Hupp, J. T.; Farha, O. K., Metal–Organic Framework Supported Single Site Chromium(III) Catalyst for Ethylene Oligomerization at Low Pressure and Temperature. *ACS Sustainable Chemistry & Engineering* **2019,** *7* (2), 2553-2557.

27. Rivera-Torrente, M.; Pletcher, P. D.; Jongkind, M. K.; Nikolopoulos, N.; Weckhuysen, B. M., Ethylene Polymerization over Metal–Organic Framework Crystallites and the Influence of Linkers on Their Fracturing Process. *ACS Catalysis* **2019,** *9* (4), 3059-3069.
28. Comito, R. J.; Wu, Z.; Zhang, G.; Lawrence III, J. A.; Korzyński, M. D.; Kehl, J. A.; Miller, J. T.; Dincă, M., Stabilized Vanadium Catalyst for Olefin Polymerization by Site Isolation in a Metal–Organic Framework. *Angewandte Chemie International Edition* **2018,** *57* (27), 8135-8139.
29. Noei, H.; Amirjalayer, S.; Müller, M.; Zhang, X.; Schmid, R.; Muhler, M.; Fischer, R. A.; Wang, Y., Low-Temperature CO Oxidation over Cu-Based Metal–Organic Frameworks Monitored by using FTIR Spectroscopy. *ChemCatChem* **2012,** *4* (6), 755-759.
30. Yousefzadeh Borzehandani, M.; Abdulmalek, E.; Abdul Rahman, M. B.; Mohammad Latif, M. A., First-principles investigation of dimethyl-functionalized MIL-53(Al) metal–organic framework for adsorption and separation of xylene isomers. *Journal of Porous Materials* **2021,** *28* (2), 579-591.
31. Ahn, S.; Nauert, S. L.; Buru, C. T.; Rimoldi, M.; Choi, H.; Schweitzer, N. M.; Hupp, J. T.; Farha, O. K.; Notestein, J. M., Pushing the Limits on Metal–Organic Frameworks as a Catalyst Support: NU-1000 Supported Tungsten Catalysts for o-Xylene Isomerization and Disproportionation. *Journal of the American Chemical Society* **2018,** *140* (27), 8535-8543.
32. Nepal, B.; Das, S., Sustained Water Oxidation by a Catalyst Cage-Isolated in a Metal–Organic Framework. *Angewandte Chemie International Edition* **2013,** *52* (28), 7224-7227.
33. Wang, L.; Wu, Y.; Cao, R.; Ren, L.; Chen, M.; Feng, X.; Zhou, J.; Wang, B., Fe/Ni Metal–Organic Frameworks and Their Binder-Free Thin Films for Efficient Oxygen Evolution with Low Overpotential. *ACS Applied Materials & Interfaces* **2016,** *8* (26), 16736-16743.
34. Kung, C.-W.; Mondloch, J. E.; Wang, T. C.; Bury, W.; Hoffeditz, W.; Klahr, B. M.; Klet, R. C.; Pellin, M. J.; Farha, O. K.; Hupp, J. T., Metal–Organic Framework Thin Films as Platforms for Atomic Layer Deposition of Cobalt Ions To Enable Electrocatalytic Water Oxidation. *ACS Applied Materials & Interfaces* **2015,** *7* (51), 28223-28230.
35. Han, W.; Li, M.; Ma, Y.; Yang, J., Cobalt-Based Metal-Organic Frameworks and Their Derivatives for Hydrogen Evolution Reaction. *Frontiers in Chemistry* **2020,** *8* (1025).
36. Peters, A. W.; Li, Z.; Farha, O. K.; Hupp, J. T., Toward Inexpensive Photocatalytic Hydrogen Evolution: A Nickel Sulfide Catalyst Supported on a High-Stability Metal–Organic Framework. *ACS Applied Materials & Interfaces* **2016,** *8* (32), 20675-20681.
37. Huang, N.-Y.; He, H.; Li, H.; Liao, P.-Q.; Chen, X.-M., A metal–organic framework with in situ generated low-coordinate binuclear Cu(i) units as a highly effective catalyst for photodriven hydrogen production. *Chemical Communications* **2020,** *56* (49), 6700-6703.
38. He, J.; Yang, H.; Chen, Y.; Yan, Z.; Zeng, Y.; Luo, Z.; Gao, W.; Wang, J., Solar Light Photocatalytic Degradation of Nitrite in Aqueous Solution Over CdS Embedded on Metal–Organic Frameworks. *Water, Air, & Soil Pollution* **2015,** *226* (6), 197.
39. Choi, H.; Peters, A. W.; Noh, H.; Gallington, L. C.; Platero-Prats, A. E.; DeStefano, M. R.; Rimoldi, M.; Goswami, S.; Chapman, K. W.; Farha, O. K.; Hupp, J. T., Vapor-Phase Fabrication and Condensed-Phase Application of a MOF-Node-Supported Iron Thiolate Photocatalyst for Nitrate Conversion to Ammonium. *ACS Applied Energy Materials* **2019,** *2* (12), 8695-8700.
40. Yang, D.; Ortuño, M. A.; Bernales, V.; Cramer, C. J.; Gagliardi, L.; Gates, B. C., Structure and Dynamics of Zr6O8 Metal–Organic Framework Node Surfaces Probed with Ethanol Dehydration as a Catalytic Test Reaction. *Journal of the American Chemical Society* **2018,** *140* (10), 3751-3759.
41. Liu, J.; Lu, Z.; Chen, Z.; Rimoldi, M.; Howarth, A. J.; Chen, H.; Alayoglu, S.; Snurr, R. Q.; Farha, O. K.; Hupp, J. T., Ammonia Capture within Zirconium Metal–Organic Frameworks: Reversible and Irreversible Uptake. *ACS Applied Materials & Interfaces* **2021,** *13* (17), 20081-20093.

42. Larabi, C.; Quadrelli, E. A., Titration of Zr3(μ-OH) Hydroxy Groups at the Cornerstones of Bulk MOF UiO-67, [Zr6O4(OH)4(biphenyldicarboxylate)6], and Their Reaction with [AuMe(PMe3)]. *European Journal of Inorganic Chemistry* **2012,** *2012* (18), 3014-3022.
43. Ouyang, M.; Cao, S.; Yang, S.; Li, M.; Flytzani-Stephanopoulos, M., Atomically Dispersed Pd Supported on Zinc Oxide for Selective Nonoxidative Ethanol Dehydrogenation. *Industrial & Engineering Chemistry Research* **2020,** *59* (6), 2648-2656.
44. Cheng, E.; Notestein, J., Catalytic dehydrogenation of isobutane over supported MoOx/K-Al2O3. *Journal of Catalysis* **2021,** *397*, 212-222.
45. Benomar, S.; Massó, A.; Solsona, B.; Issaadi, R.; López Nieto, J. M., Vanadium Supported on Alumina and/or Zirconia Catalysts for the Selective Transformation of Ethane and Methanol. *Catalysts* **2018,** *8* (4), 126.
46. Wang, X.; Zhang, X.; Pandharkar, R.; Lyu, J.; Ray, D.; Yang, Y.; Kato, S.; Liu, J.; Wasson, M. C.; Islamoglu, T.; Li, Z.; Hupp, J. T.; Cramer, C. J.; Gagliardi, L.; Farha, O. K., Insights into the Structure–Activity Relationships in Metal–Organic Framework-Supported Nickel Catalysts for Ethylene Hydrogenation. *ACS Catalysis* **2020,** *10* (16), 8995-9005.
47. Islamoglu, T.; Otake, K.-i.; Li, P.; Buru, C. T.; Peters, A. W.; Akpinar, I.; Garibay, S. J.; Farha, O. K., Revisiting the structural homogeneity of NU-1000, a Zr-based metal–organic framework. *CrystEngComm* **2018,** *20* (39), 5913-5918.
48. Lu, Z.; Liu, J.; Zhang, X.; Liao, Y.; Wang, R.; Zhang, K.; Lyu, J.; Farha, O. K.; Hupp, J. T., Node-Accessible Zirconium MOFs. *Journal of the American Chemical Society* **2020,** *142* (50), 21110-21121.
49. Peters, A. W.; Otake, K.; Platero-Prats, A. E.; Li, Z.; DeStefano, M. R.; Chapman, K. W.; Farha, O. K.; Hupp, J. T., Site-Directed Synthesis of Cobalt Oxide Clusters in a Metal–Organic Framework. *ACS Applied Materials & Interfaces* **2018,** *10* (17), 15073-15078.
50. Zhao, Y.; Truhlar, D. G., A new local density functional for main-group thermochemistry, transition metal bonding, thermochemical kinetics, and noncovalent interactions. *The Journal of Chemical Physics* **2006,** *125* (19), 194101.
51. Weigend, F.; Ahlrichs, R., Balanced basis sets of split valence, triple zeta valence and quadruple zeta valence quality for H to Rn: Design and assessment of accuracy. *Physical Chemistry Chemical Physics* **2005,** *7* (18), 3297-3305.
52. Weigend, F., Accurate Coulomb-fitting basis sets for H to Rn. *Physical Chemistry Chemical Physics* **2006,** *8* (9), 1057-1065.53. Andrae, D.; Häußermann, U.; Dolg, M.; Stoll, H.; Preuß, H., Energy-adjustedab initio pseudopotentials for the second and third row transition elements. *Theoretica chimica acta* **1990,** *77* (2), 123-141.
54. Lu, T.; Chen, Q. Shermo: A general code for calculating molecular thermochemistry properties. *Computational and Theoretical Chemistry* **2021**, 1200, 113249.
55. . I. M. Alecu, unpublished **2011**.
56. Zhao, R.; Xiao, S.; Yang, S.; Wang, X., Surface Thermolytic Behavior of Nickel Amidinate and Its Implication on the Atomic Layer Deposition of Nickel Compounds. *Chemistry of Materials* **2019,** *31* (14), 5172-5180.